Materials Today Communications 40 (2024) 109765

Contents lists available at ScienceDirect

Materials Today Communications

journal homepage: www.elsevier.com/locate/mtcomm

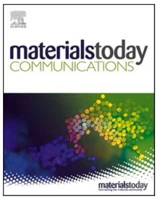

Multi- objective modeling and optimization of dissimilar laser welding by integrating an artificial intelligence predictive model with NSGA-II algorithm

Hosein Aghaei [a], Hossein Ashtari Larki [b], Milad Taqizadeh [b], Mouloud Aoudia [c], Walid Aich [d,e], Lioua Kolsi [d], Mohammad Hossein Razavi Dehkordi [b,f,*]

[a] *Department of Mechanical Engineering, Isfahan University of Technology, Isfahan, Iran*
[b] *Department of Mechanical Engineering, Najafabad Branch, Islamic Azad University, Najafabad, Iran*
[c] *Department of Industrial Engineering, College of Engineering, Northern Border University, Arar 73213, Saudi Arabia*
[d] *Department of Mechanical Engineering, College of Engineering, University of Ha'il, Ha'il 81451, Saudi Arabia*
[e] *Laboratory of Meteorology and Energy Systems, University of Monastir, Monastir 5000, Tunisia*
[f] *Aerospace and Energy Conversion Research Center, Najafabad Branch, Islamic Azad University, Najafabad, Iran*

ARTICLE INFO

Keywords:
Nickel-based alloy
Duplex 2205 steel
Laser welding
Artificial intelligence
NSGA-II algorithm

ABSTRACT

This study presents a pioneering approach in laser welding of two dissimilar materials by integrating an Artificial Intelligence (AI)-based on predictive model with the Non-dominated Sorting Genetic Algorithm II (NSGA-II) for optimizing key performance characteristics of Nickel-based alloy and duplex 2205 stainless steel. Focusing on four primary input variables including laser power, welding speed, focal distance and deviation, the research aims to predict and optimize the responses including temperature field adjacent to the melt pool, penetration depth, and tensile strength of the joint according to the experimental results. The developed AI model first accurately forecasts these characteristics based on the inputs. This predictive accuracy is critical in defining the optimal target values. Considering the multidimensional nature of the problem, where enhancing one characteristic could compromise another, the study employs a Multi-Objective Optimization (MOO) strategy. This is where the innovative integration with NSGA-II becomes pivotal. Renowned for its efficiency in navigating multiple, potentially conflicting objectives, NSGA-II assists in achieving a balanced optimization of all target parameters. This method is adept at considering the complex interdependencies among various characteristics. The novelty of this work lies in its unique combination of AI for prediction and MOO for optimization and it is for the first time that machine learning is applied on this kind of alloys with four features and four targets.

1. Introduction

In recent years, the integration of Artificial Intelligence (AI) with advanced optimization algorithms has revolutionized manufacturing processes, offering unprecedented precision and efficiency in optimizing complex systems. AI-based predictive models have demonstrated their utility across diverse engineering applications [1]. For instance, short-time wind speed prediction using artificial neural networks [2,3] and anti-noise diesel engine misfire diagnosis employing multi-scale CNN-LSTM networks [4] highlight the predictive capabilities essential for defining precise optimization targets in welding processes. The integration of NSGA-II in this study underscores its effectiveness in navigating the complex trade-offs inherent in Multi-Objective Optimization (MOO). This approach draws inspiration from advancements in fault diagnosis, such as a robust approach of multi-sensor fusion for fault diagnosis using convolutional neural networks [5,6], and dynamic neural network architectures and optimizations for predicting remaining useful life in dynamic processes [7,8]. Moreover, recent innovations in predictive accuracy algorithms, such as the alpha–beta filter enhanced by feedforward artificial neural networks for improved prediction accuracy [9], underscore the importance of precise forecasting in achieving optimal welding parameters. Similarly, advancements in fault diagnosis using non-local 1D-convolutional neural networks for rolling bearing fault diagnosis [10] and effects of heat treatment processing on microstructure evolution in alloys [11] highlight the robustness of AI techniques in complex industrial applications. Furthermore, physics-informed deep neural networks for bearing

---

* Corresponding author at: Department of Mechanical Engineering, Najafabad Branch, Islamic Azad University, Najafabad, Iran.
E-mail address: mohammadhossainrazavi@gmail.com (M.H.R. Dehkordi).

https://doi.org/10.1016/j.mtcomm.2024.109765
Received 2 April 2024; Received in revised form 26 June 2024; Accepted 4 July 2024

Nomenclature

b	Bias Term
C	Regularization Parameter
$\boldsymbol{C}$	The Box Constraint
CD	Crowding Distance
$\boldsymbol{CD_i}$	The Summation of Crowding Distances of Particle i
$\boldsymbol{d_{i,k}}$	The Crowding Distance of Particle i for the k^{th} Target Function
$\boldsymbol{F}(\boldsymbol{x})$	Multi-objective Function
$\boldsymbol{K}$	The Kernel Function
Obj 1	Temperature Duplex
Obj 2	Temperature Nickle based alloy
Obj 3	Depth of the Melt Pool
Obj 4	Tensile Strength of the Joint
$\boldsymbol{w}$	Weight Vector
x	Feature Vector
x_1	Laser Power
x_2	Welding Speed
x_3	Focal Distance
x_4	Deviation
y_i	he Actual Target Value for the ith Observation

Greek symbols

α_i	Lagrange Multiplier
ϵ	The Insensitivity Zone
$\Phi(x_i)$	The Feature Mapped Input Data
σ	Kernel Scale
$\xi_{\hat{i}}$	Slack Variable

prognosis with multisensory signals [12], and a comparative analysis of feature eliminator methods to improve machine learning [13], underscore the diversity of AI applications across different industrial domains. Additionally, microstructure and mechanical properties of thin aluminum alloy by friction stir welding [14], numerical simulation of thermal explosion welding of bimetallic plates [15], and effects of heat treatment processing on microstructure evolution and microhardness highlight advancements in materials processing techniques [16]. Laser welding has become an increasingly popular method for joining dissimilar materials due to its precision, efficiency, and ability to produce high-quality welds. Dissimilar laser welding is a modern welding technique that involves joining two or more materials with different compositions using laser energy [17]. This process is widely used in various industries, including automotive, electronics, and medical, due to its numerous advantages over traditional welding methods. Unlike conventional welding techniques, dissimilar laser welding does not require any physical contact between the materials being joined, making it a non-contact and non-damaging process. This results in minimal distortion and reduced heat-affected zones, leading to higher quality welds with less post-welding processing [18]. Additionally, the precise control of laser energy allows for the welding of dissimilar materials with vastly different melting points, making it a versatile and efficient process. Dissimilar laser welding also offers higher production speeds and improved accuracy, making it a cost-effective option for many applications [19]. As technology continues to advance, dissimilar laser welding is becoming increasingly popular and is expected to play a significant role in the future of manufacturing. In particular, the combination of Nickel-based alloy and Duplex stainless steel presents a unique challenge for welding due to their significant differences in physical and chemical properties [20]. To address this challenge, multi-objective modeling and optimization techniques have been developed, allowing for the simultaneous consideration of multiple performance criteria in the welding process. By integrating an AI predictive model with the NSGA-II algorithm, this approach offers a comprehensive and efficient way to optimize the welding process and achieve desired results. Building upon this foundation, recent studies by Nejad et al. [21] have delved into the fatigue life and welding parameter optimization of AA2024-T351 aluminum alloy, employing Artificial Neural Networks (ANNs) and multi-objective optimization algorithms to scrutinize the influence of rotational and traverse speeds on fracture toughness and fatigue crack growth rates. Furthermore, Nejad et al. [22] have contributed to the field by focusing on the fatigue life prediction of pearlitic Grade 900 A steel in railway applications. Their work involves using a feed-forward neural network to predict fatigue life based on stress cycles, occurrence and overload ratios, and conducting sensitivity analysis to gauge the impact of input parameters on fatigue life. In addition, they applied a genetic algorithm to maximize fatigue life based on the given input values. Nejad et al. [23] extended their investigations to the fatigue life of riveted joints in AA2024 aluminum alloy, employing a comprehensive approach that includes experimental tests, artificial neural networks for prediction, metaheuristic optimization for parameter calculation, and sensitivity analysis to evaluate parameter effects on the riveting process and fatigue life. These studies collectively highlight the power of combining AI-driven predictive models with optimization techniques for enhancing our understanding and control of complex material systems. In addition, experimental studies have been conducted to validate the effectiveness of these techniques and further optimize the welding process. Sołtysiak et al. [24] investigated the effect of changing the beam power in the laser welding process of Duplex Stainless Steel. Their results showed that with the increase in the power of the device, the volume of the fusion zone increases and the optimal value of the power of the device to achieve the highest power strength is 2 KW. Saravanan et al. [25] investigated the mechanical properties of the weld zone by changing the input heat to the workpiece in the Duplex stainless steel laser welding process. Their results showed that the maximum hardness in the fusion zone is due to the formation of finer grains and the corrosion rate decreases over time with the formation of an oxide layer. Mohammed et al. [26] investigated the dissimilar laser welding parameters of alloy 2205/304 stainless steel. Their results showed that with increasing laser output power, the depth and width of the weld increases and the geometry of the weld bead is also affected by the laser pulse width. Bolut et al. [27] investigated fiber laser welding of Duplex stainless steel 2205 alloy based on welding speed and input heat. Their results showed that by changing the mentioned parameters, the microstructure of the welding area will be affected, which will also affect the welding quality. Mirakhorli et al. [28] investigated the change of speed and frequency of pulse parameters in Duplex Stainless Steel laser welding process and its effect on mechanical properties. Their results demonstrated that the cooling rate, which is dependent on the change of the mentioned parameters, can be effective on the change rate of ferrite to austenite in the fusion zone. Hussein et al. [29] investigated the change of Nickel-based alloy laser welding parameters and its effect on mechanical and metallurgical properties. Their results showed that the samples welded by the laser process have a much higher hardness compared to other methods. Also, the factors affecting the cooling rate can affect the microstructure.

In conclusion, this study proposes a novel approach for optimizing key performance characteristics in dissimilar laser welding of Nickel-based alloy and Duplex stainless steel. By integrating an AI predictive model with the NSGA-II algorithm, the research aims to accurately forecast and optimize critical parameters such as temperature field near the melt pool, penetration depth, and tensile strength. The use of AI allows for precise predictions, while the incorporation of NSGA-II facilitates a balanced optimization of multiple objectives. This method is specifically tailored for the complex and multidimensional nature of materials engineering, making it a pioneering contribution to the field. This study pioneers the integration of an AI-based predictive model with the NSGA-II algorithm for optimizing laser welding of Nickel-based alloy and Duplex 2205 stainless steel, marking the first application of machine learning for these kind of material with the mentioned features and targets. It comprehensively considers four key input variables and multiple critical responses, enhancing predictive accuracy and achieving balanced optimization. The innovative approach addresses the complex interdependencies in welding dissimilar materials, opening new avenues for research and industrial applications.

2. Dissimilar laser welding experiments

Laser welding experiments were done to provide a laser welding data base for artificial neural network. The equipment's used for laser welding experiments including a 3 axis CNC table equipped with NC studio software. A continuous wave fiber laser with maximum power of 1 KW along with Raytools BW240 welding head were used for experiments. Argon gas at flow rate of 2 lit/min was applied to protect the melt pool region. All of the samples for metallography were prepared under ASTM E3. The optical microscope was used for metallography analysis to measure the melt pool depth. Evaluation of welded joint mechanical properties was performed through tensile tests applied on universal tensile testing machine. Tensile tests samples were prepared under ASTM E8 standard. The K-type thermocouples with diameter of 1 mm were used for temperature measurement. The analog signal of thermocouples grabbed by DAQ module model USB 4718. The workpiece dimensions were 20×50×1.5 mm. The chemical composition of Duplex 2205 stainless steel and Nickel-based alloy is observed in Table 1. In order to evaluate the effect of dissimilar laser welding process parameters on weld characterizations, a set of laser welding experiments at different combinations was performed to evaluate the weld characterizations. Four main parameters of laser power, welding speed, focal distance and deviation were considered as major factors. The maximum temperature at distance of 2 mm from the center of the melt pool on each alloy, depth of penetration and tensile strength were considered as means of responses. The actual and schematic view of experimental setup are shown in Fig. 1. The central composite design method was utilized for experimental design including totally 29 experiments. The experimental tests condition and the results were presented in Table 2. The provided experimental data results were used for training an AI model in order to make accurate predictions based on these datasets.

Fig. 2 illustrates the appearance of weld fusion zone cross section to measure the melt pool depth. As it is shown in Fig. 2, the weld penetration was complete and the value of depth was 1.5 mm. Furthermore, the appearance of the weld bead surface and the location of the thermocouples groove for temperature measurement are observed in Fig. 3. The appearance of tensile test samples after tensile tests for some of the experiments is depicted in Fig. 4. The tensile tests result (ultimate tensile strength and elongation rate) is depicted in Table 3. For each experimental condition, the related results gained from the tensile test condition including the ultimate tensile strength (UTS) and elongation rate is illustrated. This data was used as means the tensile tests response for training.

2.1. *The parameters effect on weld geometry*

Clearly, the heat input induced in laser welding toward material is influenced by laser beam power, the beam diameter and welding speed. All of these factors have directly impact on weld bead geometry. In other words, the laser line energy determine the efficiency of the heat input per time during laser welding process. By increasing the laser power, the penetration depth of laser beam significantly increased compared to the other factors. Additionally, the width of the weld bead clearly increased by augmentation of laser power because of creating more melt volume. The beam dimeter has a direct impact on the energy density of the beam at weld bead line. Evidently, decreasing the beam diameter reduce the weld bead width and increase the penetration depth of the weld bead. The welding speed generally determine the laser beam interaction time with material. Decreasing the welding speed simultaneously increase both depth and width of the weld bead at similar rates.

2.2. *The weld joint microstructure effect on tensile strength*

The influence of microstructure on tensile strength could be considerable. By increasing the laser beam energy, a notable microstructural transformation at different regions of the fusion zone took occur from the fusion line to the melt pool centerline. Generally, the joint tensile strength vividly depends on the melt pool dimensions and the fusion zone microstructure as well. Fig. 5 clearly depicts the variation of fusion zone microstructure in laser welding process. At the fusion zone, there are numerous regions composed of columnar dendrite and cellular dendrite microstructure. The ultimate tensile strength of columnar dendrite microstructure has been clearly in higher level while the elongation rate may be reduced. The higher laser beam energy density produced higher amount of columnar dendrite microstructure at more extended volume of the fusion zone from the fusion line to the center of the fusion zone and thereby higher tensile strength and elongation rate at wider region of melt pool depth and width is gained. At lower laser line energy, because of higher melting point of Duplex stainless steel, a wider region of unmixed zone was observed and as a results the samples failure from this region at low level of tensile strength and elongation. By increasing the laser beam energy (augmenting the laser power), the portion of columnar dendrite remarkably increased due to experiencing higher temperature gradient and thereby the tensile strength evidently increases. According to the cooling rate and intensity of the temperature gradient at different regions of the melt pool, the ratio of the columnar to cellular dendrite may change and thereby the joint tensile strength directly influenced by microstructure. On the other hand, although formation of more columnar dendrite could increase the joint tensile strength, the strain of the joint may slightly reduce compared to formation of cellular dendrite. Additionally, in dissimilar welding, due to different melting point of two materials, the joint fracture region at low levels of laser beam energy density has been toward Duplex stainless steel fusion line due to increasing the possibility of creating unmixed zone at the fusion line of Duplex stainless steel which is roots from Duplex stainless steel higher melting temperate about 80 °C.

3. Machine learning and artificial intelligence architecture

In this section the procedure of selecting the neural network according to the provided data is described.

Table 1
Materials chemical composition.

Material	Elements (%W)											
Element	C	Si	Mn	P	s	Cr	Fe	Ni	CO	AL	Ti	Mo
Duplex 2205	0.03	1	2	0.03	0.02	22	Bal	-	-			
Nickel-based alloy	0.08	0.15					2	Bal	13.5	1.5	3	4.3

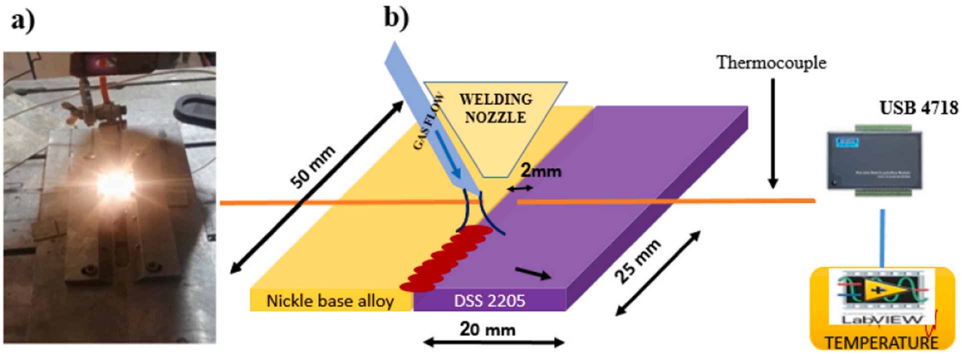

Fig. 1. Laser welding experimental configuration, a) actual view, b) schematic view.

Table 2
The laser welding experimental data.

Exp. no	Power (W)	Speed (mm/min)	Focal distance (mm)	Deviation (mm)	Temperature (℃) Nickel-based alloy	Temperature (℃) Duplex	Depth (melt pool) (mm)
1	350	300	1.5	0	116	197	1.2
2	300	200	0	-0.25	181	142	0.92
3	350	500	1.5	0	95	133	0.76
4	400	200	0	-0.25	251	302	1.5
5	350	300	1.5	0	156	170	1
6	300	400	0	-0.25	104	167	0.78
7	300	400	0	0.25	92	186	1.12
8	350	300	1.5	0.5	95	243	0.85
9	450	300	1.5	0	226	340	1.5
10	400	400	3	-0.25	235	146	1.12
11	400	200	3	-0.25	258	277	1.5
12	250	300	1.5	0	82	144	0.34
13	400	200	3	0.25	221	284	1.2
14	350	300	1.5	0	176	165	0.95
15	300	200	3	0.25	88	182	0.42
16	400	400	0	0.25	114	217	1.2
17	350	300	1.5	-0.5	180	132	0.9
18	350	300	1.5	0	144	182	1.11
19	350	300	-1.5	0	165	211	1.14
20	300	400	3	0.25	113	167	0.48
21	300	400	3	-0.25	164	137	0.37
22	350	300	4.5	0	155	122	0.45
23	350	300	1.5	0	158	187	1.15
24	400	400	0	-0.25	116	185	0.9
25	400	200	0	0.25	224	345	1.5
26	300	200	0	0.25	108	233	0.96
27	400	400	3	0.25	152	213	0.85
28	350	100	1.5	0	178	226	1.35
29	300	200	3	-0.25	105	133	0.4

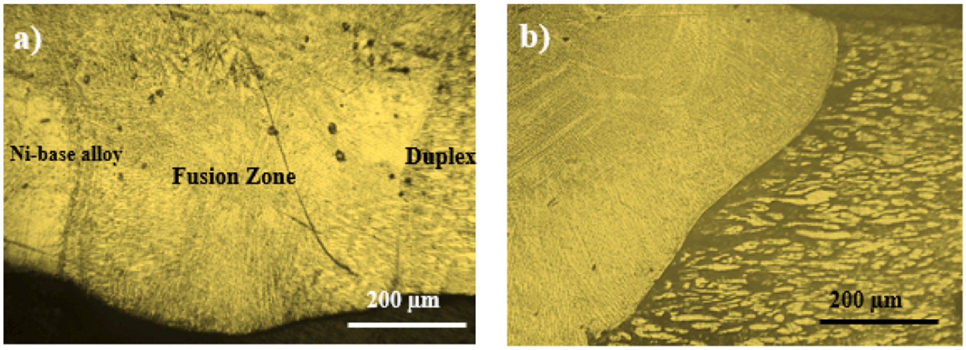

Fig. 2. The melt pool cross section appearance for depth measurement, a) dissimilar weld fusion zone and base metals, b) fusion zone adjacent to the duplex base metal.

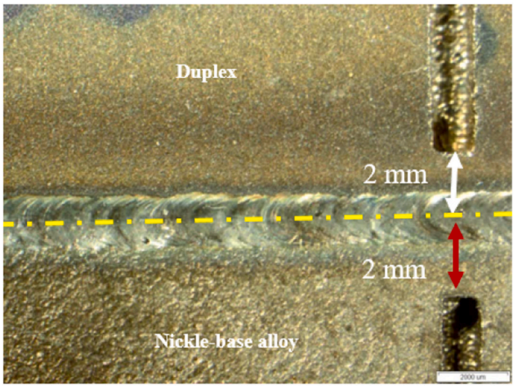

Fig. 3. Location of thermocouples placement for temperature measurement related to the weld bead center.

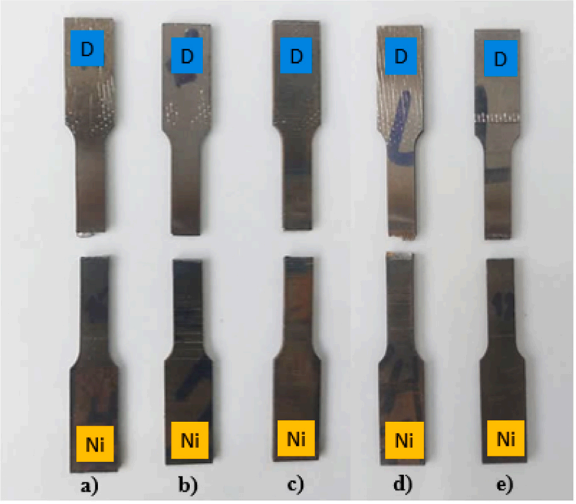

Fig. 4. Appearance of detached tensile test samples for a) Exp. No 4, b) Exp. No 6, c) Exp. No2, d) Exp. No 11, e) Exp. No7.

3.1. *Data definition and features*

In this research, the data has four features which are describes as follows.

3.1.1. *Laser power*

Laser power determines the energy delivered to the weld area, affecting temperature distribution and melt pool depth. High laser power ensures deeper penetration and a significant melt pool but can cause defects like burn-through or spatter. Optimal laser power balances penetration and material integrity.

3.1.2. *Welding speed*

Welding speed controls, the laser's movement along the weld bead. Faster speeds reduce heat input per unit length, minimizing thermal distortion and the heat-affected zone (HAZ). However, too high a speed can lead to incomplete fusion, while slower speeds increase heat input.

3.1.3. *Focal distance*

The focal distance between the laser's focal point and the workpiece surface influences the laser beam's intensity and focus. Proper adjustment ensures concentrated laser energy at the desired location, enhancing welding efficiency and quality.

Table 3
Tensile tests result of the dissimilar joint.

Exp. No	Ultimate tensile strength (UTS) (MPa)	Elongation (%)
1	245	8.1
2	229	6.2
3	205	3.2
4	326	14.2
5	275	10.3
6	209	5.1
7	228	6.6
8	210	10.4
9	312	16.1
10	267	11.1
11	291	10.3
12	186	3.2
13	246	12.2
14	262	7.3
15	248	6.1
16	293	9.2
17	218	5.4
18	251	7.1
19	295	9.2
20	212	5.5
21	185	8.9
22	228	3.3
23	266	4.4
24	256	8.3
25	308	11.3
26	274	8.4
27	258	5.8
28	285	9.3
29	234	7.2

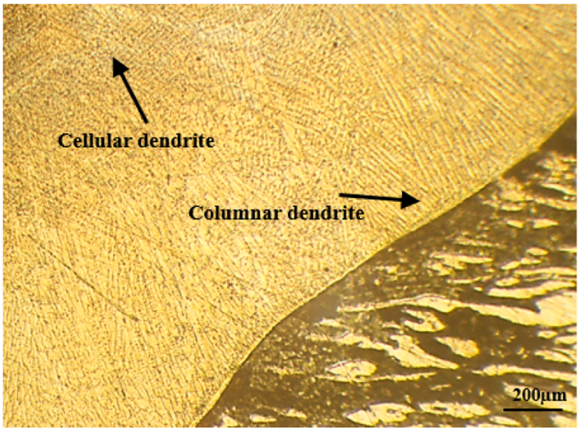

Fig. 5. The melt pool microstructure from Duplex stainless steel side to the weld centerline.

3.1.4. *Deviation*

Deviation refers to the position of the laser beam irradiation related to the center of the weld joint. In dissimilar welding this approach commonly used to balance the melting ratio of both dissimilar metals.

In this research, the primary objective is to identify a suitable AI model that can make accurate predictions based on the provided dataset. The foundation for achieving this aim lies in understanding the structure and nature of the available data. The dataset presented in Table 2, comprises multiple columns. Specifically, the initial four columns represent the input variables, which serve as the foundation for our predictions. In contrast, the subsequent four columns are the target variables, signifying the outcomes we aspire to predict. By carefully examining these inputs and targets, the study aims to derive meaningful insights and ensure the chosen AI model aligns well with the data's characteristics.

3.2. Machine learning approach

Machine learning is a subset of AI that provides systems the ability to automatically learn and improve from experience without being explicitly programmed. This involves developing algorithms that can receive input data and use statistical analysis to predict an output while updating outputs as new data becomes available. In the realm of machine learning, Support Vector Regression (SVR) stands out as a prominent methodology. SVR is an extension of Support Vector Machines (SVM), a set of related supervised learning methods primarily used for classification. While SVMs are best known for their ability to classify linear and non-linear data, their regression counterpart, SVR, adapts these principles to model and predict numerical outputs based on given input features.

3.3. Some definitions

In the following, some underlying concepts are presented.

- Hyperplane: In SVM, this is a decision boundary separating different classes. In the context of SVR, it represents a line (in two-dimensional space) or a plane in higher dimensions that best fits the data points.

- Margin: This is the gap between the hyperplane and the nearest data point from either class. Maximizing this margin is a key objective in SVM to enhance model generalization.

- Support Vectors: These are the critical elements of the data set that are closest to the hyperplane. They play a crucial role in defining the hyperplane because their removal can significantly alter the hyperplane's position, unlike other data points.

- Kernel Trick: Recognizing that real-world data is frequently not linearly separable, SVM employs the kernel trick to transform data into a higher-dimensional space, making it easier to separate linearly. Kernel functions like polynomial, radial basis function (RBF), and sigmoid are used in this transformation.

3.4. SVM and SVR

SVM and SVR are critical methodologies within the artificial intelligence and optimization landscape, offering advanced solutions for classification and regression challenges, respectively [30]. Originating from the innovative work of Vladimir Vapnik and co-authors in the 1990s [30], these algorithms are anchored in supervised learning, a subset of AI focusing on the development of predictive models based on labeled datasets. SVM is used to solve classification problems by identifying an optimal separating hyperplane, which is akin to discovering a decision boundary in a multidimensional space [30]. This boundary is meticulously calibrated to maximize the margin between the nearest data points of distinct categories, known as support vectors. The algorithm's effectiveness is significantly enhanced by its capacity to handle non-linear problems using the kernel trick [31]. This trick, a cornerstone in SVM's optimization strategy, ingeniously projects input features into a higher-dimensional space, thereby overcoming the limitations inherent in linear classifiers and enabling complex decision surfaces. SVR extends the principles of SVM to regression tasks, aiming to forecast a continuous target variable [30]. SVR's approach revolves around constructing a function that lies within an ε-insensitive zone, ensuring the deviation from actual data points is minimally confined, emphasizing model simplicity and generalization. Both SVM and SVR optimize their performance by strategically positioning training data in feature space, optimizing separation margins (in SVM) and minimizing prediction error within a specified threshold (in SVR) [32]. In Eq.1, the prediction formula is presented.

$$f(x) = w^T x + b \tag{1}$$

Where

w is the weight vector

b is the bias term

In SVR, the main objective is to minimize $\|w\|$ to ensure the model is as flat as possible, while keeping the errors within a certain threshold ϵ In a practical setting, however, it's often impossible to fit all data points within this strict margin. Therefore, slack variables ξ_i and ξ_i are introduced to allow some deviations for points outside this margin.

3.5. Problem definition

In the machine learning, the problem should be defined in a suitable format. In the following, the formulas for problem definition are presented.

3.5.1. Primal problem

In SVR, the target function is shown in Eq. 2:

$$\min \frac{1}{2}\|w\|^2 + C\sum_{i=1}^{N}(\xi_i + \xi_i) \tag{2}$$

Subject to

$$y_i - w^T \Phi(x_i) - b \le \epsilon + \xi_i$$

$$w^T \Phi(x_i) + b - y_i \le \epsilon + \xi_i$$

$$\xi_i, \xi_i \ge 0, \forall i$$

Where:

$\Phi(x_i)$ is the feature mapped input data and y_i is the actual target value for the ith observation.

C is a regularization parameter, balancing the trade-off between the flatness of $f(x)$ and the amount up to which deviations larger than ϵ are tolerated. Also, Ccan be called as the box constraint.

$\xi_i, \xi_i$are slack variables that measure the degree of violation of the ϵ margin.

ϵ is the insensitivity zone, within which no penalty is associated in the training loss.

To solve this optimization problem, a dual formulation is typically used, involving Lagrange multipliers α_i, α_i The dual form is beneficial because it simplifies the optimization problem, especially when dealing with non-linear relationships, by incorporating kernel functions and Lagrangian method which is presented in Eq. 3.

3.5.2. Lagrangian

$$L = \frac{1}{2}\|w\|^2 + C\sum_{i=1}^{N}(\xi_i + \xi_i) - \sum_{i=1}^{N}\alpha_i\left(\epsilon + \xi_i - y_i + w^T\Phi(x_i) + b\right) - \sum_{i=1}^{N}\alpha_i\left(\epsilon + \xi_i + y_i - w^T\Phi(x_i) - b\right) - \sum_{i=1}^{N}\mu_i\xi_i - \sum_{i=1}^{N}\mu_i\xi_i \tag{3}$$

Where $\alpha, \alpha$are the Lagrange multipliers.

3.5.3. Dual problem

Applying the KKT Conditions: The KKT conditions lead to a set of equations which, when substituted back into the Lagrangian, help eliminate the primal variables, the conditions are shown in Eq. 4.

$\frac{\partial L}{\partial w} = 0 \text{leads to } w = \sum_{i=1}^{N} (\alpha_i - \alpha_i) \Phi(x)$

$\frac{\partial L}{\partial b} = 0 \text{leads to } \sum_{i=1}^{N} (\alpha_i - \alpha_i) = 0$

$$\frac{\partial L}{\partial \xi_i} = 0 \text{leads to} C - \alpha_i - \mu_i = 0 \tag{4}$$

$\frac{\partial L}{\partial \xi_i} = 0 \text{leads to } C - \alpha_i - \mu_i = 0$

3.5.4. Reformulating the dual problem

After applying these conditions and simplifying, the dual problem will be obtained as Eq. 5.

$$\max \frac{-1}{2} \sum_{i=1}^{N} \sum_{i=1}^{N} (\alpha_i - \alpha_i)(\alpha_i - \alpha_i) K(x_i, x_j) - \epsilon \sum_{i=1}^{N} (\alpha_i - \alpha_i) + \sum_{i=1}^{N} y_i (\alpha_i - \alpha_i)$$

Subject to:

$$\sum_{i=1}^{N} (\alpha_i - \alpha_i) = 0$$

$$0 \le \alpha_i \quad , \quad \alpha_i \le C \quad , \quad \forall i \tag{5}$$

Where:

$K(x_i, x_j)$ is the kernel function (RBF in this case).

RBF stands for Radial Basis Function, a type of kernel which is defined as Eq. 6.

$$K(x_i, x_j) = \exp\left(-\gamma \|x_i - x_j\|^2\right) \tag{6}$$

Where x_i, x_j are the feature vectors. $\gamma$is the spread of kernel and $\|x_i - x_j\|^2$ is the squared Euclidean distance between the two feature vectors. The reason of using RBF kernel is its ability to manage non-linear relationships between the features and the target variable. The RBF kernel can map data points to a higher-dimensional space where they become linearly separable or more suitable for regression. Within the framework of this study, a four-dimensional input and output space is addressed. When dealing with such dimensional intricacy, particularly in cases of limited datasets, there emerges a significant challenge of model underfitting. Underfitting is characterized by a model's overly simplistic nature, inhibiting its capability to adequately capture and reflect the intrinsic complexities and patterns inherent in the data. This results in a model marked by high bias, evidenced by its poor performance on both training and unseen datasets, demonstrating an inability to accurately discern the true structure of the data. In contrast, the risk of overfitting is equally pertinent. This occurs when a model becomes excessively complex in its attempt to grasp data nuances, to the point where it learns not just the underlying patterns but also the noise within the training data. Such models may exhibit high accuracy on training datasets, but their practicality is compromised due to high variance. To decrease the risk of overfitting or underfitting, this study applies cross validation to find suitable values for hyper parameters including Box Constraint (C) and Kernel Scale σ.

3.6. Hyperparameters description

Box Constraint (C in SVM formula): This parameter determines the penalty imposed on observations that are positioned outside the ϵ margin (for regression tasks). It controls the trade-off between allowing training errors and forcing rigid margins. It's a regularization parameter, where a smaller value of C allows more misclassifications (or larger errors for regression) and leads to a softer margin. In contrast, a larger value of C aims for more accurate classifications (or smaller errors in regression), leading to a harder margin. In the SVM formula, this was represented as the C in the regularization term, influencing the optimization problem:

Kernel Scale (σ in the case of an RBF kernel): This hyperparameter is used in the Radial Basis Function (RBF) kernel of the SVM and affects the shape of the hyperplane. KernelScale determines how far the influence of a single training example reaches, with low values meaning 'close' and high values meaning 'far'. In other words, it defines how the similarity of any two points is calculated. In the RBF kernel, it's related to the spread of the Gaussian function. For an RBF kernel, the impact of Kernel Scale (σ) is significant in determining how the algorithm generalizes from the training data to unseen data. A smaller σ leads to a model that captures finer details of the training data (risk of overfitting), while a larger σ results in a smoother decision boundary that may generalize better on unseen data (but risk of underfitting).

3.6.1. Hyperparameter tuning using cross validation

Cross-validation is a statistical technique used to assess the performance of machine learning models. Its primary purpose is to prevent overfitting, which occurs when a model learns the training data so well that it performs poorly on new, unseen data. By using cross-validation, one can get a more realistic estimate of a model's performance on data it hasn't seen before. Cross-validation helps in identifying if a model is overfitting to the training data. In the following the Pseudocode of Cross validation is presented.

```
1. Shuffle the dataset randomly.
2. Split the dataset into k groups (or "folds").
3. For each fold:
    a. Treat the current fold as the validation set and the remaining k-1 folds as the training set.
    b. Train the machine learning model using the training set.
    c. Evaluate the model using the validation set and store the evaluation metric.
    d. Retain the model evaluation score and discard the model.
4. Summarize the skill of the model using the sample of model evaluation scores.
```

3.7. The advantages of using cross-validation

Cross validation has several advantages which are presented as follows:

- Reduced Overfitting Risk: By rotating through different subsets of the data for training and validation, cross-validation helps ensure that the model isn't simply memorizing the training data but is learning generalizable patterns. This process reduces the risk of overfitting, which is particularly important in complex models with many parameters.
- More Accurate Performance Estimate: Since the model is evaluated across multiple subsets, the performance metric is typically more reliable and less dependent on the idiosyncrasies of a single train-test split. This averaged metric offers a more balanced view of model performance.
- Model Robustness: Cross-validation tests the model's ability to adapt to various subsets of data, enhancing its robustness. A model that performs consistently well across different folds is likely to be more stable and reliable when dealing with real-world, unseen data.

Although Cross-validation increases the computational cost, but the advantages of cross- validation, overweight the drawbacks. Given the

Table 4
The optimum SVR hyperparameters for each target.

Target Name	Box Constraint	Kernel Scale
Temperature (°C)-Nickle-based alloy	995.1	3.6255
Temperature (°C)-Duplex	236.83	0.017908
Depth(mm)	186.84	4.3141
Tensile Strength (MPa)	997.76	16.341

complexity of the dataset including four distinct targets. Due to the unique nature of each target, it becomes imperative to perform cross-validation separately for every individual target. This ensures that each target receives a tailored evaluation, optimizing the model's performance for that specific output. In Table4 the best-fit values of the hyper-parameters obtained by cross validation are presented. These hyper-parameters, namely the Box Constraint and the Kernel Scale, play a pivotal role in influencing the accuracy of the model. It's these fine-tuned values that provide the foundation for the model's reliable predictive capabilities. The Bayesian optimization procedure itself incorporates the 5-fold cross-validation. For each set of hyper-parameters being evaluated, the function will perform 5-fold cross-validation and compute an averaged loss across the folds. This averaged loss is then provided as feedback to the Bayesian optimizer, which uses this information to suggest the next set of hyperparameters to try. In Table 4, the optimized hyperparameters are shown.

4. Results and discussion

In this section the results of the SVR and NSGA-II algorithm were presented in detail by considering different combination of processed data. Presentation of 35 solutions shows the potential of NSGA-II algorithm to find the optimal results with numerous configurations.

4.1. SVR Results

In Figs. 6 to 13, for each target, two plots are generated. The first one depicts the minimum objective vs. the number of function evaluations and the second one shows the objective function model for that specific target during the optimization process. These figures provide a better understanding of the model optimization.

Fig. 6 depicts Min objective versus Number of function evaluations for Temperature (℃)-Nickle based alloy. The results show that the observed and estimated minimum objectives present a clear convergence, indicating that the SVR model effectively minimized the temperature objective.

Fig. 7 shows machine learning models fine-tuned for box constraints and kernel scales, aligning with experimental data.

Fig. 8 exhibits Min objective versus Number of function evaluations for Temperature (℃)-Duplex. The rapid decline in the minimum objective reflects the SVR model's efficiency in optimizing temperature control for Duplex stainless steel.

Fig. 9 displays models optimized for box constraints and kernel scales to match experimental data.

Fig. 10 illustrates Min objective versus Number of function evaluations for Depth (mm). The model demonstrates a consistent decrease in the objective function for melt pool depth, validating the SVR model's predictive accuracy.

Fig. 11 illustrates models adjusted for box constraints and kernel scales, ensuring experimental data alignment.

Fig. 12 shows Min objective versus Number of function evaluations for Tensile strength (MPa). The steep decline in the tensile strength objective indicates that the SVR model successfully optimized this critical characteristic.

Fig. 13 demonstrates optimized box constraints and kernel scales, fitting experimental data.

These results highlight the capability of the SVR model to accurately predict and optimize complex welding parameters, forming a robust foundation for subsequent optimization.

4.2. Transition from predictive modeling to optimization

Once a predictive model is established, the next crucial step is optimizing the input parameters to achieve the best possible outcomes. This phase translates predictive insights into strategies that enhance welding efficiency and effectiveness. The input parameters—laser power, welding speed, focal distance, and deviation—significantly influence key outcomes: the temperature near the melt pool in Nickel-based alloy and Duplex 2205, the melt pool depth, and the weld joint's tensile strength. The optimization process aims to identify the best set of these parameters, requiring a multi-objective approach due to their competing nature. Multi-objective optimization finds the best trade-offs among different objectives, often visualized as a Pareto front. The NSGA-II algorithm effectively handles these conflicting objectives, providing a diverse set of optimal solutions.

4.2.1. Definition of multi-objective function

Optimization involves the process of identifying the most favorable solutions to a given problem. When dealing with multiple objective functions, particularly in scenarios where trade-offs exist among two or more competing objectives, multi-objective optimization becomes essential. This type of optimization is articulated as:

A multi-objective function can be mathematically defined as a vector of k objective functions can be shown as Eq.7.

$$F(x) = [f(x_1), f(x_2), f(x_3), \ldots, f(x_n)] \tag{7}$$

that are to be simultaneously optimized. Each objective function $f_i(x)$ maps a decision vector x from the feasible set $X \subset R^n$ to a real number, representing a distinct criterion to be optimized. Where n is the number of decision variables. In multi-objective optimization, the goal is not to find a single optimal solution but rather to identify the set of Pareto-

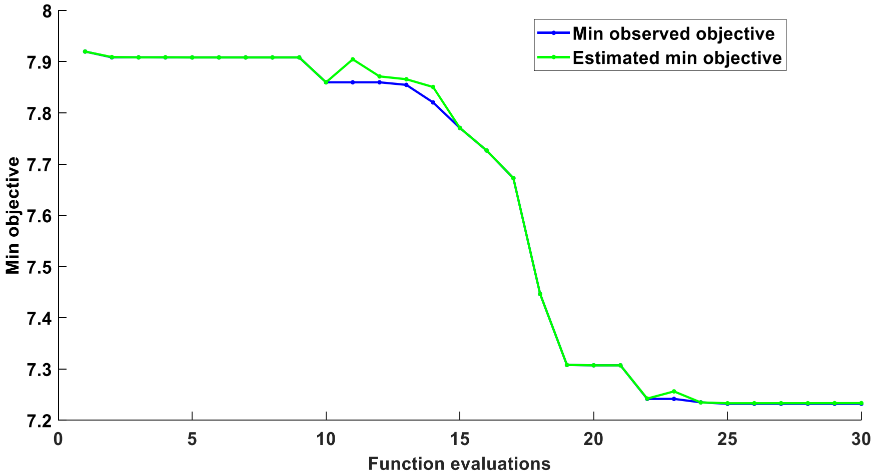

Fig. 6. Min Objective value vs. function evaluations for Temperature (℃)-Nickle based alloy.

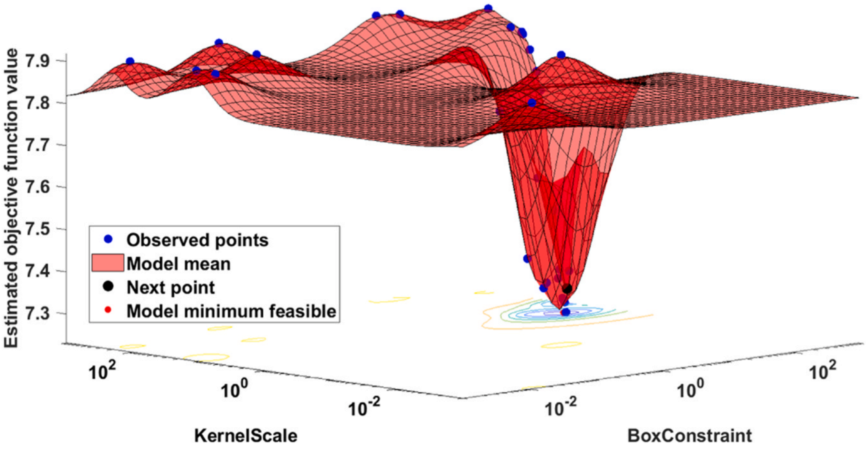

Fig. 7. Objective function model for Temperature (℃)-Nickle based alloy.

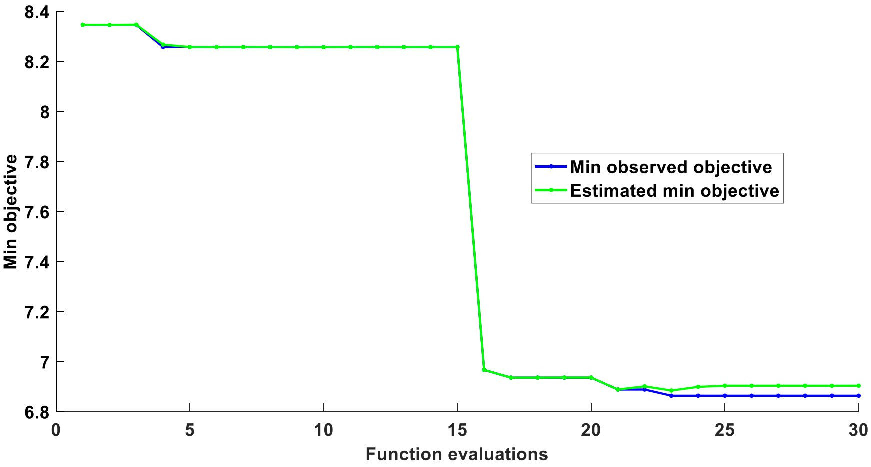

Fig. 8. Min Objective value vs. function evaluations for Temperature (℃)-Duplex.

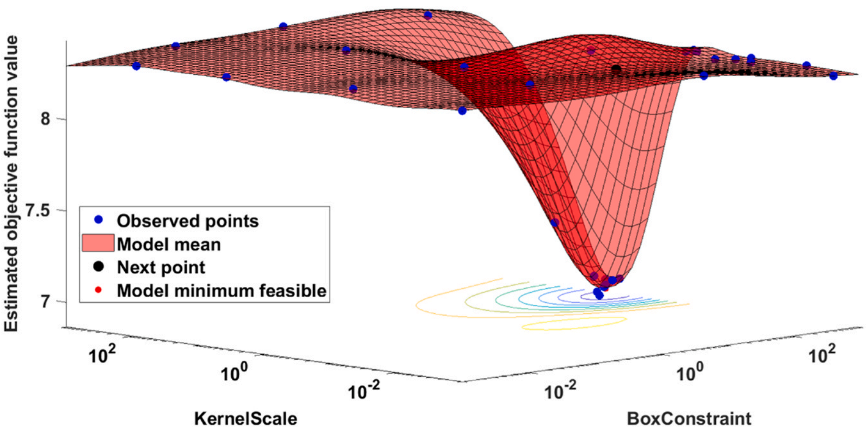

Fig. 9. Objective function model for Temperature (℃)-Duplex.

optimal solutions, where no single objective can be improved without degrading at least one of the other objectives. This formulation encapsulates the trade-offs inherent in simultaneously optimizing multiple, often conflicting, criteria, thereby directing towards solutions that best reconcile these competing objectives in a multi-dimensional decision space. One of the most common algorithms is this area is called Non-dominated Sorting Genetic Algorithm II.

4.2.2. Non-dominated sorting genetic algorithm II (NSGA-II)

The NSGA-II is an evolutionary algorithm designed for solving multi-objective optimization problems. It extends the classical genetic algorithm by introducing mechanisms for sorting solutions based on dominance and maintaining diversity. Deb et al. [33] formulation of the NSGA-II algorithm for multi-objective genetic algorithms has been fundamental. NSGAII, an evolutionary algorithm, has gained prominence for its adept application in multi-objective optimization within

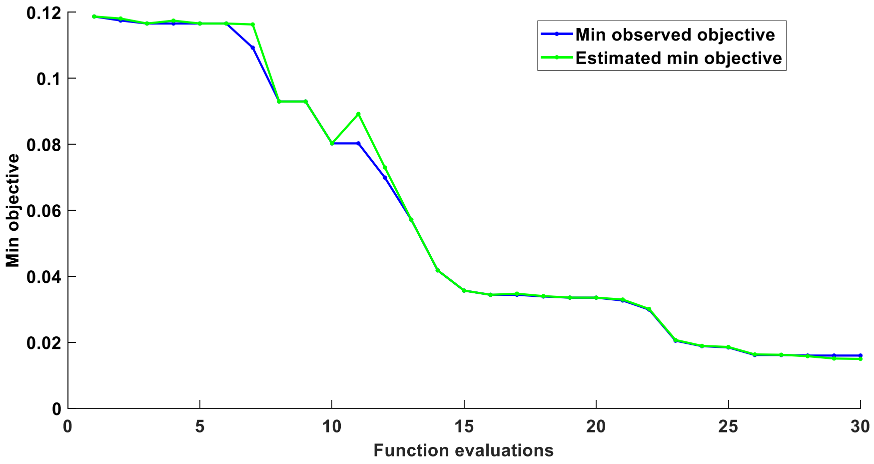

Fig. 10. Min Objective value vs. function evaluations for Depth (mm).

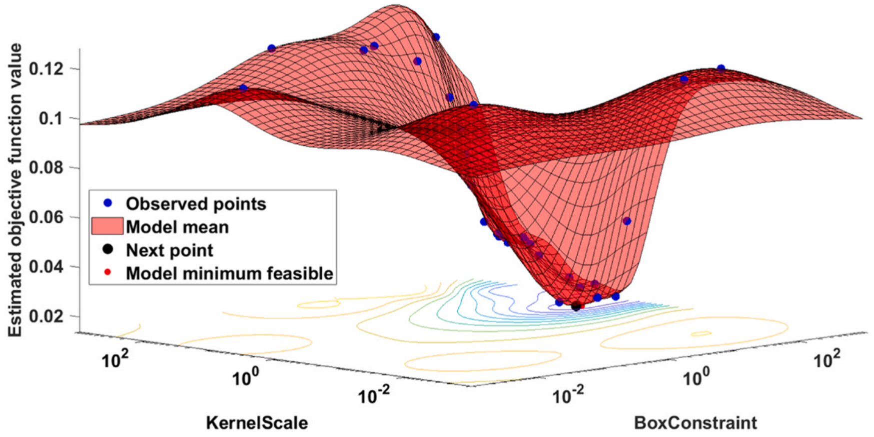

Fig. 11. Objective function model for Depth (mm).

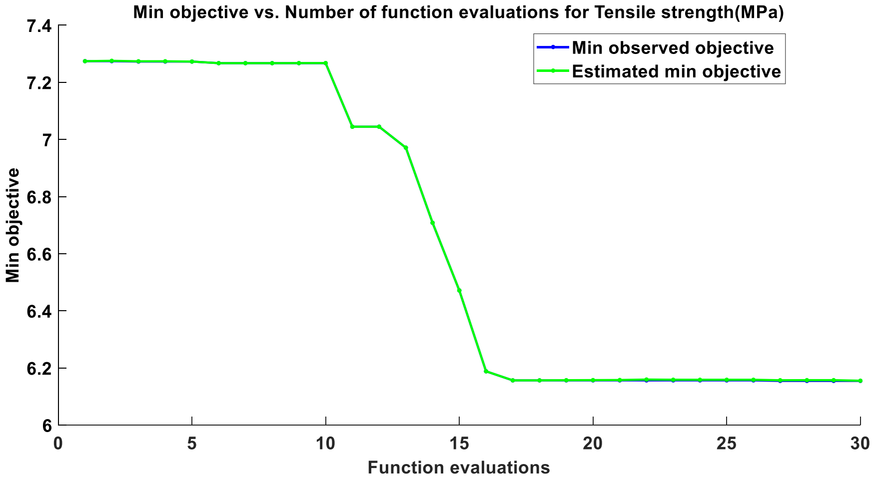

Fig. 12. Min Objective value for the fourth target.

engineering contexts. The issues of computational complexity, non-elitism, and sharing parameter dependency in earlier algorithms are resolved, employing a faster sorting mechanism and an elitist strategy. Efficient convergence to the Pareto-optimal front is ensured, and the algorithm is shown to be particularly effective in constrained multi-objective scenarios. Multi-objective optimization challenges are efficiently addressed by the robust methodology of this algorithm, which employs a multi-layered structure to ensure both diversity and efficacy in optimization processes. Researchers highlight that NSGAII's mechanisms for determining crowding distances, implementing crowded comparison operators, and executing non-dominated sorting are both rapid and straightforward, offering an edge over other multi-objective optimization techniques in ensuring diversity. Recognized as an evolutionary algorithm, NSGAII's efficiency and effectiveness are further

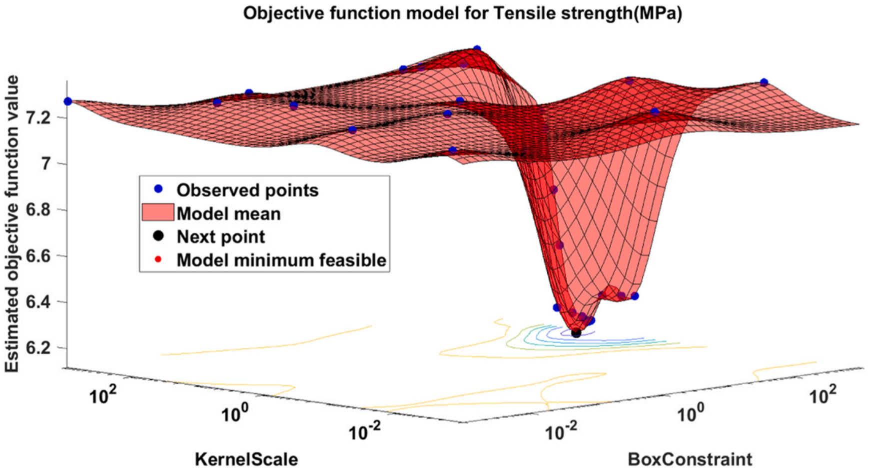

Fig. 13. Objective function model for the fourth target.

explored through key components such as Mutation. In this algorithm, each proposed solution or chromosome within the problem space comprises multiple dimensions, referred to as genes. Mutation involves the alteration of one or more of these gene values from their original state, a process crucial for introducing diversity and aiding in the discovery of novel solutions. The operational steps of NSGA_II are outlined as follows: Population Initialization, structured around variable constraints and ranges; Non-dominated Sorting, categorizing the population based on dominance criteria; Crowding Distance Calculation, applied post-sorting to assign crowding distance values and facilitating the selection of individuals based on rank and crowding distance; Selection, employing binary tournament or roulette wheel selection mechanisms inclusive of the crowded-comparison operator; Genetic Operations, utilizing Real Genetic Algorithm (GA) strategies for binary crossover and mutation processes; and Recombination and Selection, wherein the offspring population is merged with the current generation, and subsequent generation members are chosen until the population size matches that of the existing generation. Each front sequentially populates the new generation. The Pareto front, a key concept in these problems, constitutes a set of optimal non-dominated solutions in the search space, depicted through the objective function space. The optimal solutions that form the first tier in this arrangement are identified as the Pareto front. Despite the effectiveness of conventional optimization techniques, they are prone to entrapment at local optima. Moreover, the convergence efficiency of these algorithms often hinges on their initial starting points. Originating from Genetic Algorithm frameworks, NSGAII is specifically designed for multi-objective scenarios, focusing on the simultaneous optimization of each non-dominated objective. Each member of the population is compared against others in a pairwise fashion. The algorithm calculates the number of defeats each solution incurs against its counterparts. Solutions that remain undefeated in these comparisons are placed in the highest front, establishing a hierarchy of solution quality. After isolating these elite, non-dominated solutions, the algorithm repeats this sorting process for the rest. Ranking each member within their respective fronts is crucial, followed by the calculation of Crowding Distance (CD). The CD measure in the NSGAII algorithm is integral for differentiating between solutions within the same rank, particularly in a crowded front. The NSGAII algorithmic flowchart is visualized in Fig. 14.

In Fig. 15 the crowding distance for two objectives is illustrated. Also, in higher dimensions, the same meaning is valid.

Using crowding distance, prioritizes solutions with higher CDs, thereby fostering a broader spectrum of solutions. In this study, with the objective functions totaling four, the CD measure extends across a four-dimensional space, offering a nuanced approach to evaluating and optimizing a wide range of solutions. From this group, a select number (N) of superior individuals are chosen to advance to subsequent generations. This selection process emphasizes optimizing the population size beyond the initial count. For optimal performance, specific configurations of the NSGAII algorithm are necessary, detailed in Table 5.

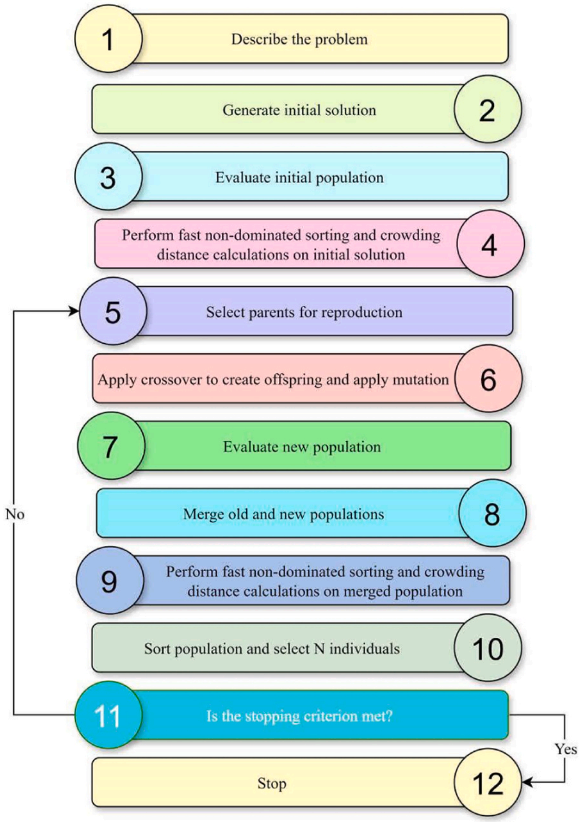

Fig. 14. The flowchart of NSGAII.

4.3. NSGA-II results and discussions

With four input variables and four target objectives, the optimal solutions are reported in Table 6.

The NSGA-II optimization process has successfully identified a set of 35 distinct solutions, corresponding to different configurations of the input vector x. Each of these solutions has been optimized to maximize

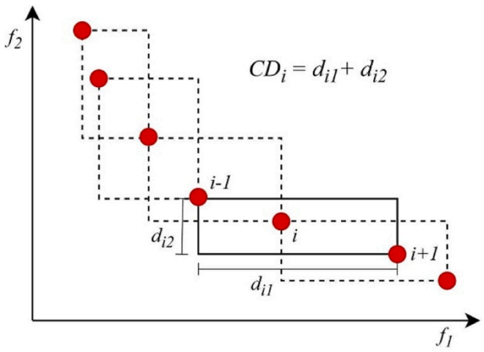

Fig. 15. The crowding distance.

Table 5
NSGA_II settings.

Setting	Value
Population Size	100
Number of Generations	400
Crossover Probability	0.8
Mutation Probability	0.025
Selection Operator	'tournament'
Crossover Operator	'intermediate'
Mutation Operator	'gaussian'

the four target functions including (Obj 1 for temperature Duplex, Obj 2 for temperature Nickle based alloy, Obj 3 for depth of the melt pool and Obj 4 for tensile strength of the joint). It's important to note that in the realm of multi-objective optimization, like that guided by NSGA-II, these solutions are part of a Pareto front. This means that while each solution excels in maximizing the target functions, they do so in varying degrees and combinations. To aid in the visualization and further analysis of these trade-offs, Fig. 16 shows a graphical view. In this figure, the trade-offs between all four target functions are illustrated for all 35 solutions.

The nature of multi-objective optimization, especially when dealing with several target functions, inherently leads to solutions that excel in different areas, reflecting diverse trade-offs among the objectives. These trade-offs are a critical aspect of the NSGA-II approach. Given the multi-dimensional nature of the optimization, no single solution can be universally considered "the best" across all objectives. Each solution might excel in one or more objectives while making concessions in others. This aspect is a fundamental characteristic of Pareto-optimal solutions where improving any one objective can only be done at the expense of another. As a result, the prioritization among these 35 solutions depends largely on the specific needs and preferences of the decision-making scenario. In Fig. 16, the Pareto fronts illustrate the trade-offs between different objectives, providing a comprehensive view of the optimization landscape.

4.4. Comparative analysis of all Pareto fronts

4.4.1. Pareto front: Obj 1 vs. Obj 2

This plot shows a clear trade-off between Objective 1 and Objective 2. As Objective 1 increases, Objective 2 generally decreases. The front demonstrates a typical Pareto optimal relationship where improving one objective leads to a deterioration in the other.

4.4.2. Pareto front: Obj 1 vs. Obj 3

This plot shows a non-monotonic relationship between Objective 1 and Objective 3. The points do not form a clear trade-off curve, indicating that the relationship between these two objectives is more complex and may have multiple regions of trade-offs.

Table 6
Optimal solutions obtained by NSGAII.

Data Number	x1	x2	x3	x4	Obj 1	Obj 2	Obj 3	Obj 4
1	449.1011	105.2673	-1.4675	-0.4995	245.2319	367.3777	1.2123	340.1254
2	449.2279	103.7722	2.1122	-0.4497	252.3585	356.3640	1.7811	321.5687
3	449.3796	104.4169	1.6600	-0.0887	232.9175	403.3410	1.8739	333.6174
4	449.2201	104.6030	4.4971	-0.4995	260.0072	311.9339	1.5470	303.9713
5	449.4992	103.9074	-1.1270	0.3749	201.4943	443.9661	1.3908	357.9487
6	449.2221	104.3889	3.7313	-0.4918	258.0454	325.9134	1.6637	309.4259
7	449.3991	104.3521	-1.4625	0.4169	198.2926	441.0248	1.3181	359.9758
8	449.5624	103.7941	-0.4284	0.3581	204.2528	445.9603	1.4756	353.5005
9	449.2679	103.9128	-0.7783	-0.2756	236.1994	400.2198	1.5302	344.6128
10	449.3725	103.9153	2.5100	-0.3244	247.0929	364.6121	1.8394	322.4059
11	449.2922	103.5741	-0.0369	-0.1231	230.4263	417.5094	1.7307	344.3728
12	449.5193	103.9421	-0.7601	-0.0399	224.2639	426.8988	1.6153	350.6622
13	449.4978	103.9532	1.8296	-0.1653	237.4050	393.4224	1.8820	330.9754
14	449.2270	104.4255	4.2546	-0.4910	259.1185	316.8519	1.5902	305.8745
15	449.2464	102.9331	4.5000	-0.4999	260.2520	312.3729	1.5458	304.1858
16	449.2278	104.0296	2.6559	-0.3824	250.2601	355.5518	1.8098	319.8001
17	449.2505	104.4794	1.9452	-0.3094	244.8545	375.2984	1.8540	326.5548
18	449.3977	103.2103	2.7205	-0.4934	256.0948	342.8604	1.7448	316.4114
19	449.4012	103.8925	-0.6370	-0.0522	225.1756	425.7487	1.6372	349.6283
20	449.2586	104.1588	1.0000	-0.2272	238.3642	397.6571	1.8351	335.0803
21	449.2213	104.4004	4.0956	-0.4970	259.0778	319.1651	1.6120	306.8044
22	449.1558	104.7331	1.6364	-0.3690	247.0208	372.3332	1.8163	326.9118
23	449.3637	104.6083	-0.4276	-0.0917	227.6718	421.6426	1.6696	347.4048
24	449.2679	104.0012	1.1889	-0.3482	245.0093	380.7152	1.7980	330.5808
25	449.4985	103.9333	-1.3903	0.4140	198.7386	441.8132	1.3287	359.6227
26	449.3537	104.6085	0.9973	-0.4520	249.6780	368.8663	1.7062	328.5410
27	449.2767	105.1670	1.0862	-0.3748	245.9410	378.0732	1.7715	330.3051
28	449.4176	103.5967	-0.1581	0.0388	221.7500	433.0303	1.7073	348.4371
29	449.1358	105.5439	-0.6662	-0.4837	246.6478	371.1325	1.3975	336.7165
30	449.2225	104.5939	3.3786	-0.4940	257.3558	331.6258	1.7009	311.7231
31	449.3935	103.9259	1.4267	-0.3076	243.6234	383.2239	1.8368	330.2360
32	449.3763	104.0396	2.2244	-0.1722	238.6504	385.4870	1.8738	327.9412
33	449.2177	105.1708	1.1434	-0.4964	252.1011	361.1645	1.6851	326.0297
34	449.3975	104.6592	-1.5000	0.4573	196.0180	439.8507	1.2804	360.2017
35	449.1759	104.9301	3.0263	-0.4958	256.5898	337.0145	1.7276	313.9650

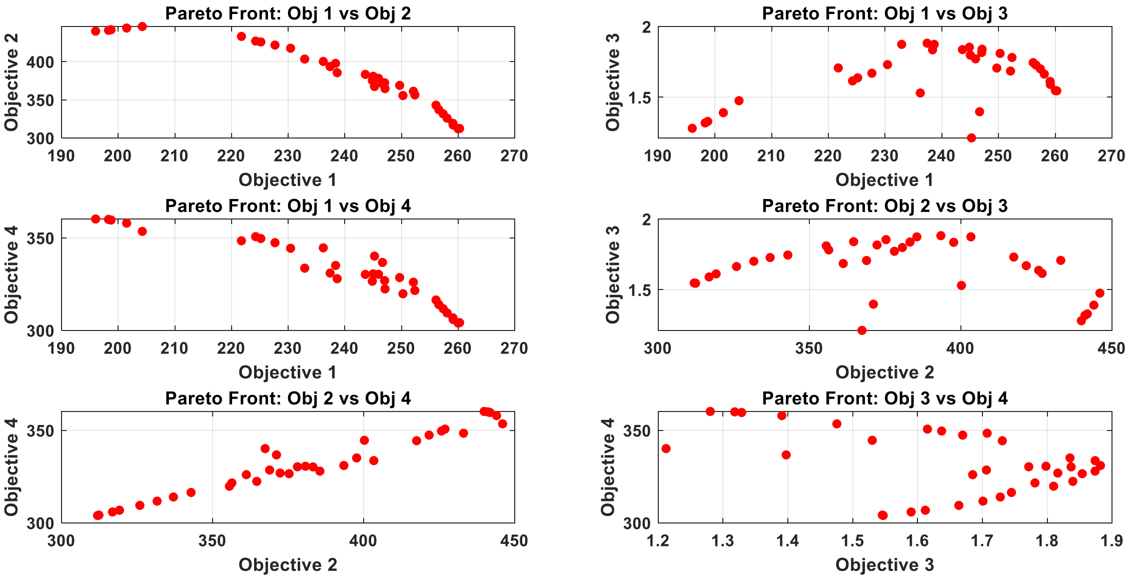

Fig. 16. All Pareto fronts of four objectives.

4.4.3. *Pareto front: Obj 1 vs. Obj 4*

This plot shows a clear trade-off between Objective 1 and Objective 4. As Objective 1 increases, Objective 4 tends to decrease, forming a well-defined Pareto front similar to the first plot, where one objective is sacrificed for the improvement of the other.

4.4.4. *Pareto front: Obj 2 vs. Obj 3*

This plot shows a non-monotonic relationship between Objective 2 and Objective 3, with some segments where both objectives improve together and others where they trade-off. This indicates a complex interplay between these two objectives with no single trend dominating the Pareto front.

4.4.5. *Pareto front: Obj 2 vs. Obj 4*

This plot shows a complex Pareto front where the relationship between Objective 2 and Objective 4 is not straightforward. Initially, both objectives improve together up to a certain point, after which further improvement in Objective 2 leads to a deterioration in Objective 4.

4.4.6. *Pareto front: Obj 3 vs Obj 4*

This plot shows a non-monotonic Pareto front between Objective 3 and Objective 4. The trade-offs are not consistent, with some regions where improvements in one objective correlate with improvements in the other, and other regions where trade-offs become evident. This reflects a multifaceted relationship between these objectives.

The analysis of the six Pareto fronts highlights the varied and intricate nature of the trade-offs between different objectives. While some pairs of objectives exhibit clear and straightforward trade-offs, others demonstrate complex and non-linear relationships. Understanding these dynamics is crucial for effective decision-making in multi-objective optimization, as it allows for a more nuanced approach to balancing competing objectives and finding the most suitable trade-offs based on specific goals and constraints.

5. Conclusion

This study focused on the dissimilar laser welding of Nickel-based alloy and Duplex 2205 stainless steel to create a comprehensive dataset for process modeling and optimization. The input parameters included laser power, welding speed, focal distance, and deviation, while the target outputs were Temperature- Nickel-based alloy, temperature- Duplex, Melt pool depth, and Tensile strength. Integrating Support Vector Regression (SVR) with the Non-dominated Sorting Genetic Algorithm II (NSGA-II) for multi-objective optimization yielded significant results. One of the key achievements of this study was the development of precise predictive models through SVR. These models were finely tuned using Bayesian optimization and cross-validation techniques to ensure high accuracy and reliability. The SVR models accurately predicted the target outputs based on the given input parameters, providing a robust tool for understanding the relationships between different welding parameters and outcomes. Through the application of the NSGA-II, the study identified 35 optimal input configurations. These configurations form a Pareto front of solutions that balance the four target objectives: Temperature- Nickel-based alloy, Temperature- Duplex, Melt pool depth, and Tensile strength. The Pareto front represents the trade-offs between these objectives, allowing decision-makers to choose the most suitable configurations based on their needs and priorities. The comprehensive dataset created in this study includes a wide range of input parameters and corresponding outputs, enabling detailed process modeling. This dataset is invaluable for further research and development in laser welding, as it provides a solid foundation for understanding how different parameters affect welding quality and performance. Integrating advanced modeling techniques ensures that the insights gained are deep and actionable. The combination of SVR and NSGA-II represents a sophisticated approach to multi-objective optimization. SVR provides the predictive accuracy needed to model complex relationships, while NSGA-II offers a powerful method for exploring the trade-offs between multiple objectives. This integration ensures the optimization process is thorough and efficient, leading to high-quality solutions that can significantly improve welding processes. The solutions identified in this study allow decision-makers to navigate complex trade-offs effectively. Understanding the Pareto front will enable them to make informed choices that align with specific industrial and research needs. For instance, if a higher tensile strength is required, they can choose configurations that achieve this at the expense of other objectives like melt pool depth or temperature control. The study's outcomes highlight the importance of precise heat input control. By optimizing laser power, welding speed, focal distance, and deviation, it is possible to achieve superior weld quality. This study's advanced modeling and optimization techniques demonstrate their effectiveness in reaching these goals, providing a clear pathway for improving welding processes in industrial applications.

Future works

Some possible future works can be applying the identified optimal welding parameters and predictive models for real-time adjustments to enhance weld quality and performance in practical applications. Also, extending the methodology to other materials and welding processes, refining models and algorithms, and integrate them into industrial systems for real-time optimization and adaptive control, thereby improving precision, flexibility, and overall welding efficiency.

CRediT authorship contribution statement

Lioua Kolsi: Software, Writing – review & editing. **Mouloud Aoudia:** Investigation, Software, Writing – review & editing. **Walid Aich:** Software, Writing – review & editing. **Milad Taqizadeh:** Methodology, Investigation, Formal analysis. **Mohammad Hossein Razavi Dehkordi:** Writing – original draft, Supervision, Resources. **Hosein Aghaei:** Resources, Formal analysis, Conceptualization. **Hossein Ashtari Larki:** Writing – review & editing, Writing – original draft, Software.

Declaration of Competing Interest

The authors declare that they have no known competing financial interests or personal relationships that could have appearedl to influence the work reported in this paper.

Data availability

Data will be made available on request.

Acknowledgment

The authors extend their appreciation to the Deanship of Scientific Research at Northern Border University, Arar, KSA for funding this research work through the project number “NBU-FFR–2024–1475–06".

References

[1] J. Wang, Z. Sun, L. Gu, H. Azimy, Investigating the effect of laser cutting parameters on the cut quality of Inconel 625 using response surface method (RSM), Infrared Phys. Technol. 118 (2021) 103866, https://doi.org/10.1016/j.infrared.2021.103866.

[2] X. Zheng, et al., Short-time wind speed prediction based on Legendre multi-wavelet neural network, CAAI Trans. Intell. Technol. 8 (3) (2023) 946–962, https://doi.org/10.1049/cit2.12157.

[3] H. Azimy, N. Azimy, A.H. Meghdadi Isfahani, S.A. Bagherzadeh, M. Farahnakian, Analysis of thermal performance and ultrasonic wave power variation on heat transfer of heat exchanger in the presence of nanofluid using the artificial neural network: experimental study and model fitting, J. Therm. Anal. Calorim. 148 (16) (2023) 8009–8023, https://doi.org/10.1007/s10973-022-11827-1.

[4] C. Qin, et al., Anti-noise diesel engine misfire diagnosis using a multi-scale CNN-LSTM neural network with denoising module, CAAI Trans. Intell. Technol. 8 (3) (2023) 963–986, https://doi.org/10.1049/cit2.12170.

[5] B. Peng, et al., 3D-STCNN: spatiotemporal convolutional neural network based on EEG 3D features for detecting driving fatigue, J. Data Sci. Intell. Syst. (2023), https://doi.org/10.47852/bonviewJDSIS3202983.

[6] J. Sun, X. Gu, J. He, S. Yang, Y. Tu, C. Wu, A robust approach of multi-sensor fusion for fault diagnosis using convolution neural network, J. Dyn., Monit. Diagn. (2022) 103–110, https://doi.org/10.37965/jdmd.2022.95.

[7] S.A. Bagherzadeh, D. Asadi, Detection of the ice assertion on aircraft using empirical mode decomposition enhanced by multi-objective optimization, Mech. Syst. Signal Process.. 88 (2017) 9–24, https://doi.org/10.1016/j.ymssp.2016.11.013.

[8] S. Simani, et al., Dynamic neural network architecture design for predicting remaining useful life of dynamic processes, J. Data Sci. Intell. Syst. (2023), https://doi.org/10.47852/bonviewJDSIS3202967.

[9] J. Khan, E. Lee, K. Kim, A higher prediction accuracy–based alpha–beta filter algorithm using the feedforward artificial neural network, CAAI Trans. Intell. Technol. 8 (4) (2023) 1124–1139, https://doi.org/10.1049/cit2.12148.

[10] H. Wang, Z. Liu, T. Ai, Long-range dependencies learning based on non-local 1D-convolutional neural network for rolling bearing fault diagnosis, J. Dyn., Monit. Diagn. 1 (3) (2022) 148–159, https://doi.org/10.37965/jdmd.2022.53.

[11] L.I. Luyao, R.E.N. Luying, Y.A.N. Zhaoming, et al., Effects of heat treatment processing on microstructure evolution and microhardness of deformed Mg Gd Y Zn Zr alloys, J. Ordnance Equip. Eng. 44 (10) (2023) 72–77.

[12] X. Chen, M. Ma, Z. Zhao, Z. Zhai, Z. Mao, Physics-informed deep neural network for bearing prognosis with multisensory signals, J. Dyn., Monit. Diagn. 1 (4) (2022) 200–207, https://doi.org/10.37965/jdmd.2022.54.

[13] J. Tanimu, S. Shiaeles, M. Adda, A comparative analysis of feature eliminator methods to improve machine learning phishing detection, J. Data Sci. Intell. Syst. (2023), https://doi.org/10.47852/bonviewJDSIS32021736.

[14] L.I.U. Xiuru, W.U. Xia, C.H.E.N. Dajun, et al., Microstructure and mechanical properties of thin aluminum alloy by friction stir welding, J. Ordnance Equip. Eng. 44 (11) (2023) 229–234.

[15] M.I.A.O. Guanghong, M.A. Qiuyue, H.U. Yu, et al., Numerical simulation of thermal explosion welding of tungsten copper bimetallic plates, J. Ordnance Equip. Eng. 44 (8) (2023) 257–265.

[16] Y. Zhang, M. Hossein Razavi Dehkordi, M. Javad Kholoud, H. Azimy, Z. Li, M. Akbari, Numerical modeling of the temperature distribution and melt flow in dissimilar fiber laser welding of duplex stainless steel 2205 and low alloy steel, Opt. Laser Technol. 174 (2024) 110575, https://doi.org/10.1016/j.optlastec.2024.110575.

[17] C. Sun, M.H.R. Dehkordi, M.J. Kholoud, H. Azimy, Z. Li, Systematic evaluation of pulsed laser parameters effect on temperature distribution in dissimilar laser welding: a numerical simulation and artificial neural network, Opt. Laser Technol. 163 (2023) 109407, https://doi.org/10.1016/j.optlastec.2023.109407.

[18] M. Azari, E. Rasti, M.H.R. Dehkordi, H. Azimy, A. Zarei, S.A. Bagherzadeh, Investigation of temperature distribution and melt pool microstructure in laser fusion welding of Inconel 625 superalloy, J. Laser Appl. 33 (2021) 2, https://doi.org/10.2351/7.0000376.

[19] M.J.H. Rawa, M.H. Razavi Dehkordi, M.J. Kholoud, N.H. Abu-Hamdeh, H. Azimy, Using the numerical simulation and artificial neural network (ANN) to evaluate temperature distribution in pulsed laser welding of different alloys, Eng. Appl. Artif. Intell. 126 (2023) 107025, https://doi.org/10.1016/j.engappai.2023.107025.

[20] A.K. Maurya, C. Pandey, R. Chhibber, Dissimilar welding of duplex stainless steel with Ni alloys: a review, Int. J. Press. Vessels Pip. 192 (2021) 104439, https://doi.org/10.1016/j.ijpvp.2021.104439.

[21] R.M. Nejad, N. Sina, D.G. Moghadam, R. Branco, W. Macek, F. Berto, Artificial neural network based fatigue life assessment of friction stir welding AA2024-T351 aluminum alloy and multi-objective optimization of welding parameters, Int. J. Fatigue 160 (2022) 106840, https://doi.org/10.1016/j.ijfatigue.2022.106840.

[22] R.M. Nejad, N. Sina, W. Ma, Z. Liu, F. Berto, A. Gholami, Optimization of fatigue life of pearlitic Grade 900 A steel based on the combination of genetic algorithm and artificial neural network, Int. J. Fatigue 162 (2022) 106975, https://doi.org/10.1016/j.ijfatigue.2022.106975.

[23] R.M. Nejad, N. Sina, W. Ma, Z.W. Song, S.P. Zhu, R. Branco, W. Macek, A. Gholami. Artificial neural network based fatigue life assessment of riveted joints in AA2024 aluminum alloy plates and optimization of riveted joints parameters. Int. J. Fatigue. vol. 178, p. 107997. https://doi.org/10.1016/j.ijfatigue.2023.107997.

[24] R. Sołtysiak, T. Giętka, A. Sołtysiak, The effect of laser welding power on the properties of the joint made of 1.4462 duplex stainless steel, Adv. Mech. Eng. 10 (1) (2018), https://doi.org/10.1177/1687814017751949.

[25] S. Saravanan, K. Raghukandan, N. Sivagurumanikandan, Pulsed Nd: YAG laser welding and subsequent post-weld heat treatment on super duplex stainless steel, J. Manuf. Process. 25 (2017) 284–289, https://doi.org/10.1016/j.jmapro.2016.12.015.

[26] G. Ridha Mohammed, M. Ishak, S.N.A.S. Ahmad, H.A. Abdulhadi, Fiber laser welding of dissimilar 2205/304 stainless steel plates, Metals 7 (12) (2017) 546, https://doi.org/10.3390/met7120546.

[27] M. Bolut, C.Y. Kong, J. Blackburn, K.A. Cashell, P.R. Hobson, Yb–fibre laser welding of 6 mm duplex stainless steel 2205, Phys. Procedia 83 (2016) 417–425, https://doi.org/10.1016/j.phpro.2016.08.043.

[28] F. Mirakhorli, F. Malek Ghaini, M.J. Torkamany, Development of weld metal microstructures in pulsed laser welding of duplex stainless steel, J. Mater. Eng. Perform. 21 (10) (2012) 2173–2176, https://doi.org/10.1007/s11665-012-0141-3.

[29] N.I.S. Hussein, I.R. Pashby, D.G. McCartney, Laser and arc weld methods for direct metal deposition of Waspaloy, Int. J. Manuf. Technol. Manag. 17 (4) (2009) 419–425, https://doi.org/10.1504/IJMTM.2009.023958.

[30] V. Vapnik, The Nature of Statistical Learning Theory, Springer science & business media, 1999.

[31] C. Cortes, V. Vapnik, Support-vector networks, Mach. Learn. 20 (1995) 273–297, https://doi.org/10.1007/BF00994018.

[32] D.P. Kingma, J. Ba, Adam: a method for stochastic optimization, arXiv Prepr. arXiv 1412 (2014) 6980.

[33] K. Deb, A. Pratap, S. Agarwal, T. Meyarivan, A fast and elitist multiobjective genetic algorithm: NSGA-II, IEEE Trans. Evol. Comput. 6 (2) (2002) 182–197, https://doi.org/10.1109/4235.996017.